Nano Research 2018, 11(9): 4806–4822
https://doi.org/10.1007/s12274-018-2066-0
Research Article
ISSN 1998-0124
CN 11-5974/O4

Tumor microenvironment-responsive hyaluronate-calcium carbonate hybrid nanoparticle enables effective chemotherapy for primary and advanced osteosarcomas

Yi Zhang[1,2,§], Lulu Cai[3,§], Di Li[1,§], Yeh-Hsing Lao[4], Dingzhuo Liu[2], Mingqiang Li[4,5] (✉), Jianxun Ding[1] (✉), and Xuesi Chen[1]

[1] *Key Laboratory of Polymer Ecomaterials, Changchun Institute of Applied Chemistry, Chinese Academy of Sciences, Changchun 130022, China*
[2] *Department of Orthopedics, the Fourth Affiliated Hospital of China Medical University, Shenyang 110032, China*
[3] *Personalized Drug Therapy Key Laboratory of Sichuan Province, Hospital of the University of Electronic Science and Technology of China, Sichuan Provincial People's Hospital, Chengdu 610072, China*
[4] *Department of Biomedical Engineering, Columbia University, New York, NY 10027, USA*
[5] *Guangdong Provincial Key Laboratory of Liver Disease, The Third Affiliated Hospital of Sun Yat-sen University, Guangzhou 510630, China*
[§] *Yi Zhang, Lulu Cai, and Di Li contributed equally to this work.*

Received: 30 January 2018
Revised: 24 March 2018
Accepted: 25 March 2018

KEYWORDS

hybrid nanomedicine, tumor-acidity responsiveness, controlled drug delivery, multi-stage osteosarcoma, chemotherapy

ABSTRACT

Osteosarcoma is the most common malignancy in the bone. Current chemotherapy offers limited efficacy with significant side effects, especially for advanced and relapsed osteosarcomas. Nanoparticle-formulated chemotherapeutic drugs may be used to resolve these issues, but several aspects of these formulations remain unsatisfactory, such as how to improve their stability in the bloodstream, prevent undesirable drug leakage, and enhance targeted drug accumulation in the tumor. In this study, a tumor microenvironment-responsive calcium carbonate ($CaCO_3$)-crosslinked hyaluronate (HA) nanoparticle was prepared via a "green" process to effectively deliver doxorubicin (DOX) for the treatment of various stages of osteosarcoma. The DOX-loaded hyaluronate-calcium carbonate hybrid nanoparticle (HA-DOX/$CaCO_3$) demonstrated superior stability both *in vitro* and *in vivo*, and rapidly released DOX at the tumor site when triggered by the acidic tumor microenvironment. Compared with free DOX and a non-crosslinked nanoparticle (HA-DOX), HA-DOX/$CaCO_3$ exhibited the most potent inhibition efficacy toward both primary and advanced models of murine osteosarcoma, resulting in effective tumor inhibition, improved survival time, and reduced adverse effects. Most importantly, in the advanced osteosarcoma model, HA-DOX/$CaCO_3$ potently suppressed tumor growth by 84.6%, which indicates the potential of this platform for osteosarcoma treatment, particularly for advanced and relapsed cases. The proposed polysaccharide nanoparticle would be a promising drug delivery platform to advance osteosarcoma nanomedicine.

Address correspondence to Jianxun Ding, jxding@ciac.ac.cn; Mingqiang Li, ml3777@columbia.edu

1 Introduction

Osteosarcoma is the most common bone malignancy in children and young adults, and owing to its high heterogeneity, patients usually suffer from disease recurrence, early systemic metastasis, and poor quality of life [1–3]. Although chemotherapy significantly improves the outcomes of patients with localized osteosarcoma, the treatments for advanced, relapsed, and metastatic osteosarcomas remain unsatisfactory, and the five-year survival rate of these patients has remained unchanged in the past few decades [4]. Furthermore, conventional chemotherapy is always accompanied by significant side effects, such as hypersensitivities, gastrointestinal toxicity, and myelosuppression, which may hinder its translation [5–7]. The limited therapeutic efficacy and serious side effects of conventional chemotherapeutic drugs might be attributable to their intrinsic limitations, such as poor water solubility, short blood circulation time, insufficient tumor accumulation, and uncontrolled drug release. As a result, there is a clear need to design a superior and more efficient drug formulation for osteosarcoma therapy.

In the past decade, with the development of nanotechnology and material science, more nanoparticle-formulated drug delivery systems have emerged for cancer nanomedicine to tackle the aforementioned obstacles [8–11]. These advanced systems, such as carbon nanotubes [12, 13], liposomes [14], polymer nanoparticles, and nanogels [15–18], demonstrate numerous benefits, including better control of drug release, improved bioavailability, prolonged circulation half-life, enhanced permeation and retention (EPR), and reduced toxicity-related side effects. Hence, it is believed that these nanoparticle-formulated drug delivery platforms may have superior performance to improve the therapeutic outcome against cancer. However, there are still many barriers that limit the translation of these nanomedicine systems. For example, for these drug-loaded nanoparticles, their stability in the blood circulation and their abilities of targeted drug release are two major issues influencing their antitumor efficacies and side effects [19]. Insufficient stability of drug-loaded nanoparticles may result in significant drug leakage in the blood circulation to induce undesirable, serious side effects. Moreover, to enhance therapeutic effects, the nanoparticles need to possess superior abilities of targeted drug release so that the chemotherapy drugs could be delivered to the tumor site. To deal with these two major obstacles, a series of nanoparticles, including *in situ* crosslinking and stimuli-responsiveness, has been developed and reported [19, 20]. Although a few nanoparticle-formulated drug delivery platforms have been reported to tackle these issues, there is still room to further improve the efficacy. For instance, for most of the reported platforms, their poor size uniformities, low drug-loading contents, and usage of toxic organic solvents may decrease their performance in cancer treatment.

Calcium compounds, such as calcium phosphate ($Ca_3(PO_4)_2$) and calcium carbonate ($CaCO_3$), have received increasing attention for nanomedicine applications because of their excellent biocompatibility and biodegradability [21–24]. Furthermore, it has been demonstrated that calcium crosslinking or mineralization of polymer micelles could enhance the stability of nanoparticles [25–27] and make the nanoparticles sensitive to the acidic tumor microenvironment [28–30].

Herein, aiming to overcome the aforementioned obstacles on drug delivery, a pH-sensitive hyaluronate (HA) nanoparticle was designed to deliver doxorubicin (DOX) by introducing $CaCO_3$ as a crosslinker for the treatment of various stages of osteosarcoma. Compared to the widely used synthetic polymers, HA, as a natural polysaccharide, offers better security for *in vivo* studies with potential for clinical translation owing to its excellent biocompatibility and biodegradability [24, 31, 32]. DOX is one of the most widely used antitumor drugs in clinical settings, and has revealed excellent antitumor effects for a wide range of malignant tumors [33, 34]. Additionally, DOX possesses stable fluorescence performance, making it a favorable probe for real-time tracing and quantitative analysis [35–37]. The synthetic process of the DOX-loaded nanoparticle (designated HA-DOX/$CaCO_3$) is presented in Scheme 1. In brief, an aqueous DOX solution was added to an HA solution under stirring to generate HA-DOX nanoparticle based on electrostatic interactions between cationic DOX and the anionic carboxyl moieties of HA. Subsequently, Ca^{2+} solution was added to the above solution, and then an aqueous solution of CO_3^{2-} was added drop-wise to induce ionic supersaturation, triggering the development of $CaCO_3$ crosslinking [28]. Through effective crosslinking, HA-DOX/$CaCO_3$

may possess enhanced stability in the blood circulation due to its more compact structure with the HA shell and $CaCO_3$ core. Moreover, owing to the acid-responsive $CaCO_3$ core, HA-DOX/$CaCO_3$ would exhibit sensitive pH-responsiveness to the decreased pH from the physiological condition (pH 7.4) to the tumor microenvironment (pH 6.8) or intracellular endosomal/lysosomal condition (pH 5.5) [38, 39]. Taking these two advantages into consideration, HA-DOX/$CaCO_3$ may have the capability of increasing the circulation time and improving tissue penetrability, thereby facilitating cancer cell uptake and the intracellular release of DOX. Based on this presupposition, HA-DOX/$CaCO_3$ was believed to display superior antitumor efficiency in a K7 osteosarcoma-allografted BALB/c mouse model as well as in the advanced-stage model. To verify the hypothesis, the drug release, cell internalization, cytotoxicity, *in vitro* hemolysis, pharmacokinetic profile, biodistribution, *in vivo* antitumor efficacy, and safety of HA-DOX/$CaCO_3$ were systematically investigated. To guarantee the stringency of this study, the non-crosslinked DOX-loaded HA nanoparticle (HA-DOX) was synthesized as a control and evaluated along with HA-DOX/$CaCO_3$ for all experiments.

2 Results and discussion

2.1 Preparation and characterization of $CaCO_3$-crosslinked, DOX-loaded HA nanoparticles

HA is a biocompatible, biodegradable, and non-toxic polysaccharide, which has been widely used for drug delivery [40]. In this study, HA was first utilized to interact with DOX via electrostatic adsorption owing to its carboxyl groups on the side chain. After loading with DOX to form an HA-DOX complex (HA-DOX), Ca^{2+} and CO_3^{2-} were subsequently introduced to complete the *in situ* crosslinking and to obtain HA-DOX/$CaCO_3$ (Scheme 1). All syntheses were performed in aqueous medium, indicating no potential deleterious effects caused by the introduction of toxic reagents or organic solvents [41]. As shown in Figs. 1(a) and 1(d), the hydrodynamic radii (R_hs) of HA-DOX and HA-DOX/$CaCO_3$ were 58.8 and 88.5 nm, respectively. Both drug-loaded complexes were under the size criteria of the EPR effect (~ 100 nm), indicating their potential for passive drug delivery [42]. Furthermore, the results were consistent with the transmission electron microscope (TEM) results, which further confirmed the particle sizes

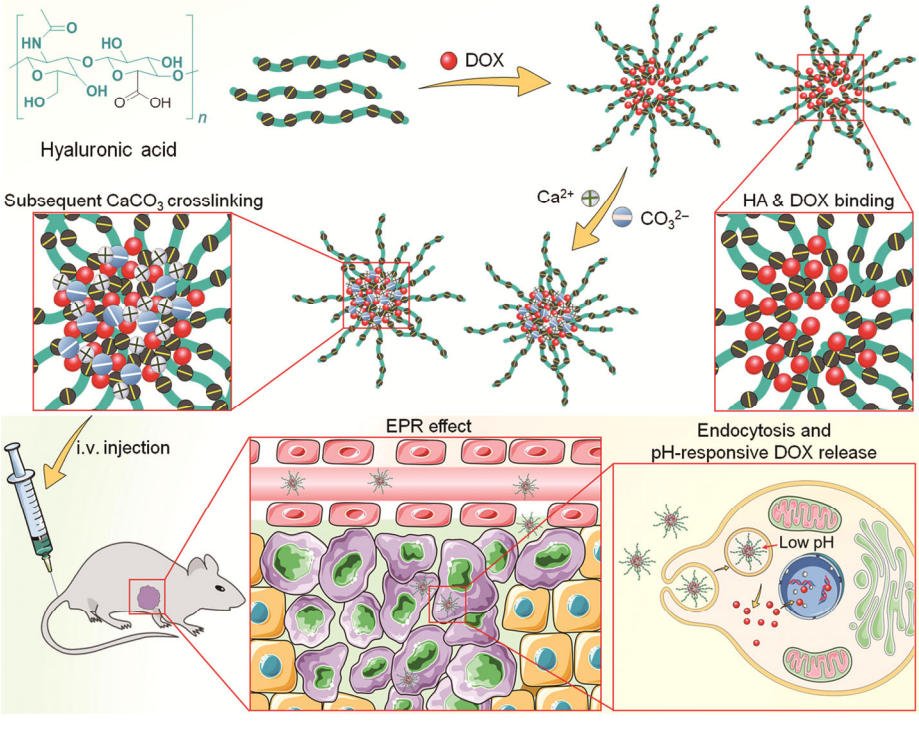

Scheme 1 Schematic illustration for preparation, intravenous injection, *in vivo* circulation, selective accumulation in tumor tissue, and pH-triggered intracellular drug release of HA-DOX/$CaCO_3$.

of HA-DOX and HA-DOX/$CaCO_3$ (Figs. 1(b) and 1(e)). To confirm the $CaCO_3$ crosslinking, the elementary compositions of HA-DOX and HA-DOX/$CaCO_3$ were verified using energy-dispersive X-ray (EDX) spectroscopy. The EDX spectrum of HA-DOX/$CaCO_3$ revealed strong signal energy peaks in the range of 3.62–3.78 keV, characteristic of Ca, indicating formation of the $CaCO_3$ core for *in situ* crosslinking (Figs. 1(c) and (f)). In addition, as presented in Fig. S2 in the Electronic Supplementary Material (ESM), the zeta potentials of HA-DOX and HA-DOX/$CaCO_3$ were slightly negative (−8.7 ± 0.7 and −2.2 ± 0.5 mV, respectively) under the physiological condition, implying good dispersion stability, because of lower potential of non-specific interactions with serum proteins. This could prolong their circulation time in the bloodstream and potentially facilitate tumor accumulation [43, 44].

To verify if the $CaCO_3$ crosslinking could enhance the stability of the nanoparticles, the size changes of the drug-loaded nanoparticles with and without $CaCO_3$ were measured in bovine serum albumin (BSA) solution (30.0 mg·mL^{-1}) for 48 h (Fig. S1(a) in the ESM). HA-DOX obviously aggregated during incubation with BSA protein, while no notable size increase was observed for HA-DOX/$CaCO_3$. Quantitatively, after 48-h incubation, the size of HA-DOX increased by 2.2 times. However, for HA-DOX/$CaCO_3$, its size only increased by less than 9%, demonstrating the enhanced stability of HA-DOX/$CaCO_3$. The enhanced stability of HA-DOX/$CaCO_3$ was further confirmed in 10% fetal bovine serum (FBS). As shown in Fig. S1(b) in the ESM, there was no significant change in the size distribution of HA-DOX/$CaCO_3$, within 48-h incubation, but HA-DOX was much larger. The results are consistent with those observed in the BSA solution (Fig. S1(a) in the ESM), confirming the enhanced stability after $CaCO_3$ crosslinking. The pH-responsiveness of HA-DOX and HA-DOX/$CaCO_3$ was then confirmed by monitoring the size changes in phosphate-buffered saline (PBS) under different pH conditions (pH 7.4, 6.8, and 5.5). As shown in Figs. 1(g) and 1(h), HA-DOX and HA-DOX/$CaCO_3$ exhibited similar trends in size changes under the same condition (pH 5.5 > pH 6.8 > pH 7.4), indicating that DOX encapsulation and the $CaCO_3$ crosslinking did not affect the pH sensitivity. However, under the neutral condition (pH 7.4), the size change of HA-DOX/$CaCO_3$ was less than that of HA-DOX during the 48-h incubation period. The enhanced stability and higher stimuli-response sensitivity are likely conferred by the $CaCO_3$ crosslinking, and the results demonstrate its potential for drug delivery as it was highly stable in the normal physiological condition and would go through rapid swelling as well as drug release once the nanoparticle reached an acidic microenvironment, especially inside the tumor tissue or endosomal compartment.

2.2 *In vitro* drug release and inhibition of cell proliferation

The DOX release profiles from HA-DOX and HA-DOX/$CaCO_3$ were next evaluated under different pH conditions. As shown in Fig. 1(j), HA-DOX/$CaCO_3$ showed a delayed release of DOX at pH 7.4, while the release profile was significantly accelerated under acidic pH conditions (pH 6.8 and 5.5). At pH 7.4, the cumulative amount of released DOX from HA-DOX/$CaCO_3$ was 25.7% ± 5.1% after 72 h. In contrast, the nanoparticle could release 49.0% ± 5.5% and 89.7% ± 6.4% of the DOX at pH 6.8 and 5.5, respectively. In other words, compared with the neutral condition, the amount of DOX released at pH 6.8 and 5.5 was 2.2 and 4.1 times higher, respectively. HA-DOX showed similar results at pH 6.8 and 5.5 (60.5% ± 6.2% and 81.1% ± 6.8%; Fig. 1(i)), which were 1.4 and 1.9 times higher than the amount detected at pH 7.4 (42.5% ± 5.4%). As aforementioned, compared with HA-DOX, HA-DOX/$CaCO_3$ was more compact at pH 7.4, but was more relaxed under lower pH conditions (pH 6.8 and 5.5).

It should be noted that HA-DOX showed a significant initial burst release at all three tested pH conditions compared to HA-DOX/$CaCO_3$. This might be due to the fact that the structure of HA-DOX was relatively unstable, and the $CaCO_3$ crosslinking further enhanced the pH sensitivities of the nanoparticles. When decreasing the pH from 7.4 to 5.5, a significant boost on DOX release was observed, showing again that HA-DOX/$CaCO_3$ could enhance drug release in the tumor microenvironment or intracellularly.

The cell internalization and intracellular drug release of HA-DOX and HA-DOX/$CaCO_3$ were monitored on murine osteosarcoma K7 cells using confocal laser scanning microscopy (CLSM) and flow cytometry (FCM). As shown in Fig. 2(a), after 2-h incubation, the DOX

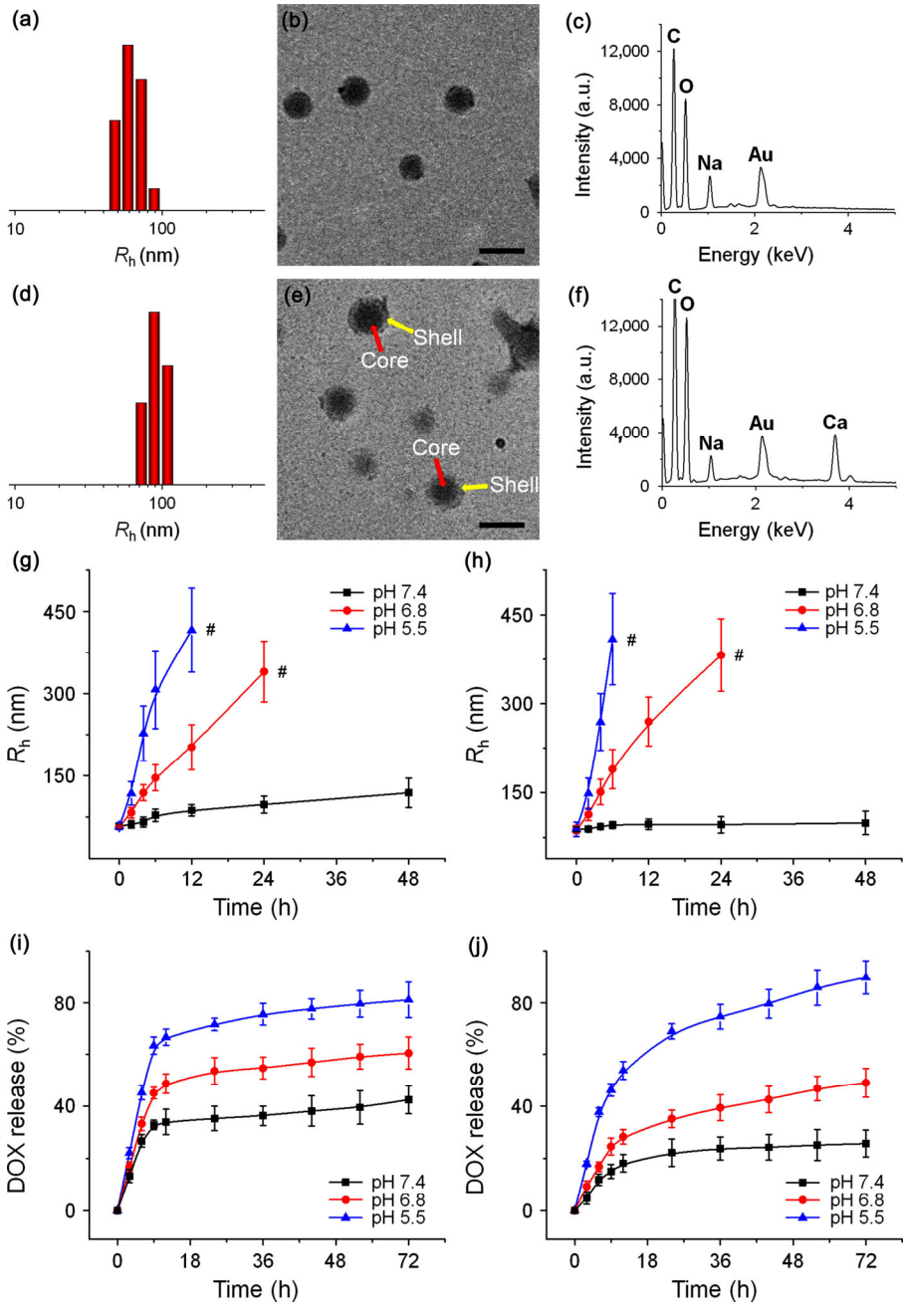

Figure 1 Physicochemical properties and release behaviors of HA-DOX and HA-DOX/$CaCO_3$. (a)–(f) Hydrodynamic radius distributions, morphologies, and EDX spectra of (a)–(c) HA-DOX and (d)–(f) HA-DOX/$CaCO_3$. Scale bar: 200 nm. (g) and (h) R_h changes of (g) HA-DOX and (h) HA-DOX/$CaCO_3$ in PBS at various pH values vs. time. (i) and (j) Release profiles of DOX from (i) HA-DOX and (j) HA-DOX/$CaCO_3$ in PBS at various pH values. All statistical data are represented as mean ± standard deviation (n = 3 for (g)–(j)).

fluorescence in the cells treated with HA-DOX or HA-DOX/$CaCO_3$ was lower than that detected with free DOX. However, after 6-h incubation, higher DOX fluorescence was clearly detected in the cells treated with the two DOX-loaded nanoparticles compared with that of the free DOX group. This difference might be related to their different cell internalization mechanisms. As a previous study demonstrated, free DOX enters cells by simple diffusion [45], whereas the two types of DOX-loaded nanoparticles are taken up by the tumor cells via the endocytosis pathway and subsequently become ensnared in endosomal/lysosomal compartments, which are maintained in an acidic condition. Compared with HA-DOX or HA-DOX/$CaCO_3$, the cells treated

with free DOX exhibited stronger DOX fluorescence after a short incubation time (2 h) on account of a faster internalization processing. In addition, due to the self-quenching effect, free DOX could have a higher fluorescence intensity compared with those of the DOX-loaded nanoparticles at the same concentration [46]. Nevertheless, within the two nanomedicine groups, similar DOX fluorescence intensities could be observed at 2 h, while HA-DOX/$CaCO_3$ showed a higher DOX fluorescence intensity at 6 h post-treatment because of its enhanced stability and better acid-responsive DOX release intracellularly. It is worth mentioning that DOX, as an anthracycline-based topoisomerase II (TOP2)-inhibitor, exhibits its antitumor effects through its ability to modify DNA [47–49]. On account of the fast DOX–DNA binding, the DOX signal is mainly located in the nuclei [50–52]. The intracellular internalization of free DOX, HA-DOX, or HA-DOX/$CaCO_3$ was further verified by FCM. As shown in Figs. 2(b) and 2(c), the cells treated with free DOX displayed the highest fluorescence intensity at 2 h. After 6-h incubation, however, the fluorescence intensities of DOX were ranked as HA-DOX/$CaCO_3$ > HA-DOX > free DOX, which was consistent with the trend detected by CLSM.

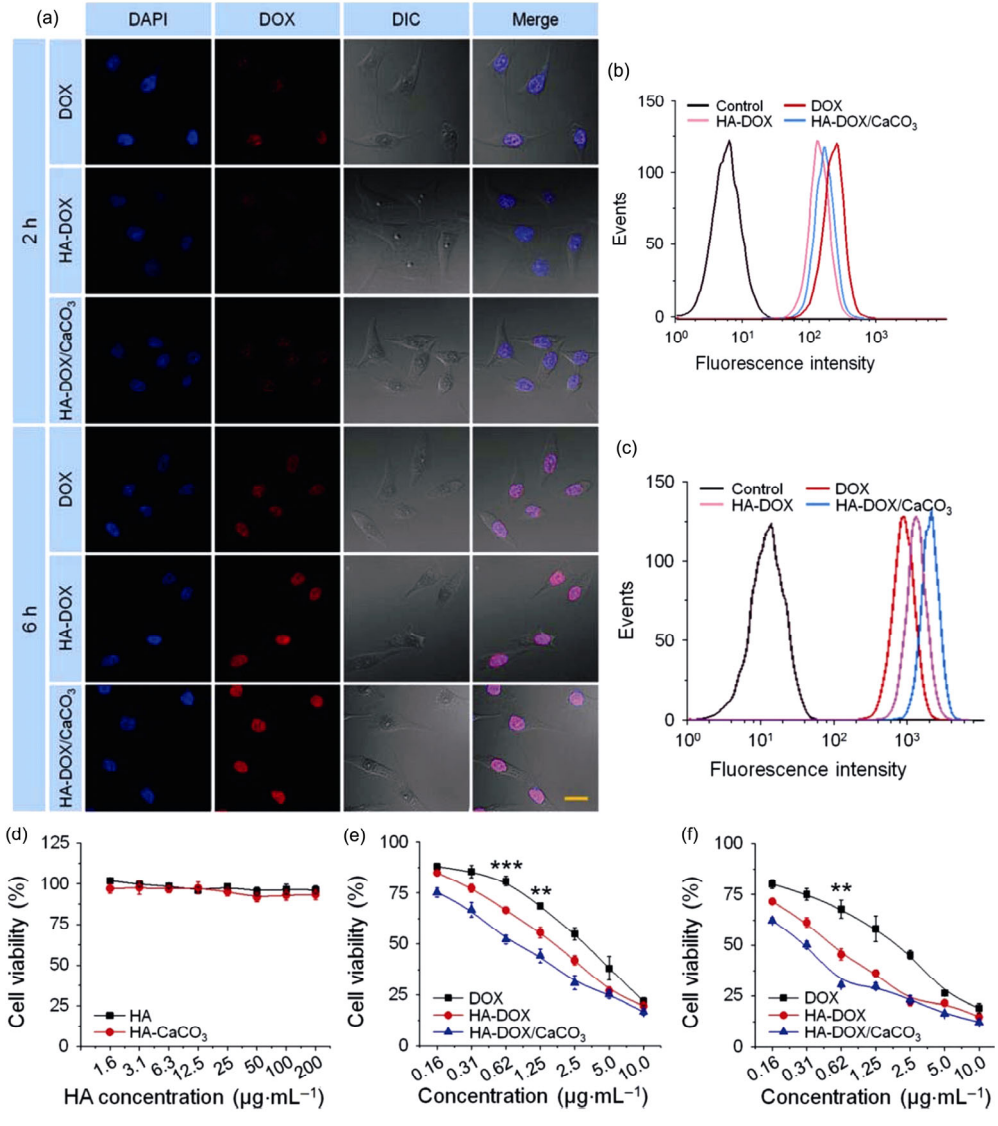

Figure 2 Cell uptake and cytotoxicity. (a) CLSM and ((b) and (c)) FCM analyses of K7 cells after incubation with free DOX, HA-DOX, and HA-DOX/$CaCO_3$ for (b) 2 h or (c) 6 h. Scale bar: 20.0 μm. (d) *In vitro* cytotoxicity of HA and HA-$CaCO_3$ against K7 cells after incubation for 48 h. (e) and (f) *In vitro* cytotoxicities of free DOX, HA-DOX, and HA-DOX/$CaCO_3$ to K7 cells after incubation for (e) 24 h or (f) 48 h. Data are presented as mean ± standard deviation (n = 3 for (d)–(f); $^{**}P < 0.01$, $^{***}P < 0.001$).

The biocompatibility of HA and HA-$CaCO_3$ was evaluated on K7 cells using a methyl thiazolyl tetrazolium (MTT) assay with the same concentration of HA ranging from 1.6 to 200 μg·mL^{-1}. After 48 h of incubation, no significant inhibition of cell proliferation was observed at any of the tested concentrations (Fig. 2(d)), indicating the superior biocompatibility of HA and HA-$CaCO_3$ for biomedical applications. Subsequently, cell proliferation assays were carried out to determine the *in vitro* cytotoxicities of HA-DOX and HA-DOX/$CaCO_3$ against K7 cells. As shown in Figs. 2(e) and 2(f), the K7 cell proliferation of all groups was inhibited in a dose- and time-dependent manner. Compared with free DOX and HA-DOX at the same drug concentration, HA-DOX/$CaCO_3$ revealed the highest inhibitory effect at both 24 and 48 h post-treatment. This was consistent with the CLSM and FCM results (Figs. 2(a) and 2(b)). As shown in the CLSM and FCM data, HA-DOX/$CaCO_3$ enabled more efficient DOX delivery, and the treated cells accumulated higher amounts of DOX, which would lead to the enhanced apoptosis of cancer cells. Specifically, the half-maximal inhibitory concentration (IC_{50}) values of free DOX, HA-DOX, and HA-DOX/$CaCO_3$ were 2.6, 1.5, and 0.9 μg·mL^{-1} at 24 h, respectively. In other words, HA-DOX/$CaCO_3$ improved the inhibition of cancer cell proliferation by 2.9 and 1.7 times compared with free DOX and HA-DOX, respectively. Moreover, when prolonging the incubation time to 72 h, the IC_{50} of HA-DOX/$CaCO_3$ was further reduced to 0.3 μg·mL^{-1}, which was 5 and 2 times lower than the IC_{50} values of free DOX (1.5 μg·mL^{-1}) and HA-DOX (0.6 μg·mL^{-1}). This excellent inhibition performance on cell proliferation implied that HA-DOX/$CaCO_3$ might have outstanding potential for chemotherapy applications and exhibit better antitumor efficacy *in vivo*.

2.3 *In vivo* pharmacokinetics and biodistribution

Stability in the bloodstream directly affects the efficacy of nanomedicine systems; undesired drug dissociation, leakage, or unpacking of nanoparticles may reduce the efficacy and induce undesired side effects. Thus, the prolonged blood circulation and deferred blood clearance of nanomedicines are significant for efficient drug delivery to the targeted tumor site [53, 54]. In our study, the plasma pharmacokinetic profiles of free drug and nanomedicines were determined by high-performance liquid chromatography analyses. As shown in Fig. 3(a), the DOX-loaded nanoparticles, especially HA-DOX/$CaCO_3$, exhibited significant enhancement in blood circulation time compared with free DOX. Specifically, for the HA-DOX/$CaCO_3$ group, the maximum concentration (C_{max}) of DOX was 4.27 μg·mL^{-1}, while those of the HA-DOX and free DOX groups were 3.37 and 2.60 μg·mL^{-1}, respectively. Furthermore, the half-life periods of free DOX, HA-DOX, and HA-DOX/$CaCO_3$ were 10.4, 15.1, and 23.5 h, respectively. Compared with free DOX, a higher original DOX concentration and a slower rate of DOX decay of the drug-loaded nanoparticles might be due to the protection from drug encapsulation. Benefiting from the enhanced stability, HA-DOX/$CaCO_3$ displayed better behavior in the blood circulation compared to HA-DOX. Moreover, the area under the concentration vs. time curve from 0 to the final time (AUC_{0-t}) of DOX was 16.7 μg·h^{-1}·mL^{-1} in the HA-DOX/$CaCO_3$ group, which was 1.9 or 5.2 times higher than that of the HA-DOX group (8.6 μg·h^{-1}·mL^{-1}) or the free DOX group (3.2 μg·h^{-1}·mL^{-1}). The significantly improved pharmacokinetics of HA-DOX/$CaCO_3$ might be attributed to its superior stability after crosslinking.

To estimate the biodistribution, *ex vivo* fluorescence imaging of isolated solid tumors and main organs at 6 and 12 h post-injection was carried out in the K7 osteosarcoma-bearing BALB/c mice. As shown in Fig. 3(c), remarkable DOX fluorescence was observed in the liver and kidney of each group at 6 and 12 h post-injection. This can be explained by the fact that the liver and kidney are two of the main organs responsible for drug digestion and metabolism [55, 56]. Due to their nanoparticle structures, HA-DOX and HA-DOX/$CaCO_3$ were gradually eliminated from the body. Thus, at 6 h, most of the free DOX might be eliminated by the kidney, while HA-DOX can be in the process of elimination by the kidney at that time [57–59]. This might result in different drug distributions in the kidney between the free DOX group and HA-DOX group. DOX fluorescence in the kidney of the group treated with HA-DOX/$CaCO_3$ was lower than that of the HA-DOX group at 6 h post-injection. The reason could be that the $CaCO_3$ crosslinking enhanced the stability in the blood circulation by stabilizing the nanoparticle structure. This reduced the amount of dissociated DOX from the nanoparticles, which was easily drained away from the kidney. When comparing

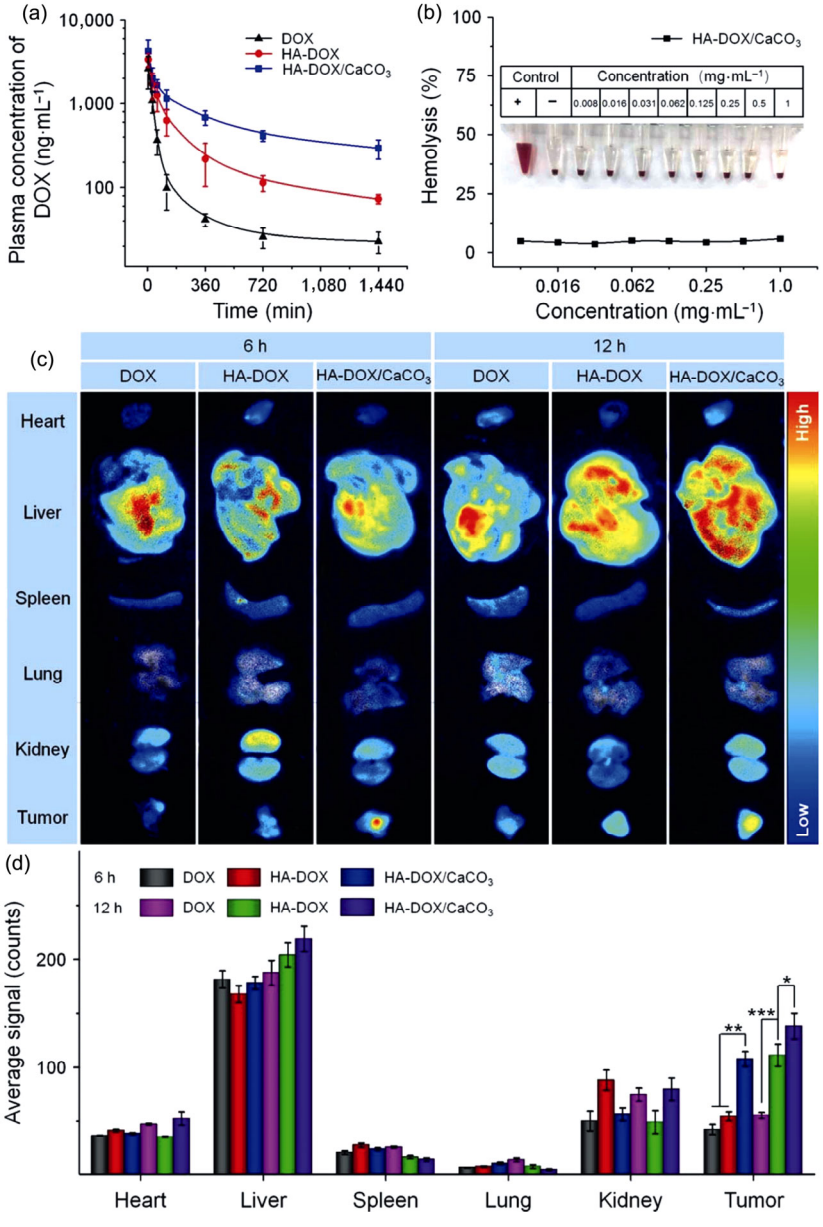

Figure 3 *In vivo* pharmacokinetics, hemolysis, and biodistribution. (a) *In vivo* pharmacokinetic profiles of free DOX, HA-DOX, or HA-DOX/$CaCO_3$ in mice. (b) Hemolytic activity of HA-DOX/$CaCO_3$. (c) *Ex vivo* DOX fluorescence images and (d) average signals of tumors and organs (the heart, liver, spleen, lung, and kidney) at 6 or 12 h post-injection of free DOX, HA-DOX, or HA-DOX/$CaCO_3$ into K7 osteosarcoma-allografted BALB/c mice. Data are presented as mean ± standard deviation (n = 3 for (a) and (d); *P < 0.05, **P < 0.01, ***P < 0.001).

the DOX intensity in tumors within these three groups, the mice treated with free DOX showed the lowest DOX accumulation, and the HA-DOX/$CaCO_3$ group showed a significantly higher DOX intensity than the other groups at both 6 h (P < 0.001) and 12 h (P < 0.05) post-injection. Both the reduced elimination by the kidney and the EPR effect allowed for the nanoparticle formation to improve DOX accumulation in the tumor. Moreover, because of the enhanced stability conferred by $CaCO_3$ crosslinking, prolonged circulation time was observed to significantly increase DOX accumulation in the tumor. The fluorescent intensity was further semi-quantitatively analyzed using Maestro™ 2.4 software (Cambridge Research and Instrumentation Inc., Woburn, MA, USA). The fluorescence intensity of the tumor in the HA-DOX/$CaCO_3$ group was 2.1 or 1.8 times higher than that of the free DOX or HA-DOX group at 6 h post-injection, respectively (Fig. 3(d)). At 12 h

after administration, the intensity of the HA-DOX/$CaCO_3$ group was still the highest, which was 2.6 or 1.3 times higher than that of the free DOX or HA-DOX group, respectively. These results indicated that HA-DOX/$CaCO_3$ could adequately enhance the drug accumulation in the tumor tissue with reduced premature drug release.

2.4 *In vivo* antitumor efficacy

The $CaCO_3$ crosslinking enhanced the HA nanoparticle with better stability, drug release profiles, intracellular drug delivery, cytotoxicity, and biodistribution. We next asked whether HA-DOX/$CaCO_3$ is a promising candidate for further preclinical evaluations. First, the *in vivo* antitumor efficacies of drug-loaded nanoparticles were evaluated in a primary osteosarcoma model, the K7 osteosarcoma-allografted BALB/c mouse model. As shown in Fig. 4(a), when the tumor volume reached approximately 50 mm^3, free DOX, HA-DOX, or HA-DOX/$CaCO_3$ was administrated intravenously every four days for a total of six injections at an equivalent dosage of 5.0 $mg \cdot kg^{-1} \cdot BW^{-1}$ of DOX, and PBS was used as a control. As presented in Fig. 4(b), the PBS group exhibited a rapid increase in average tumor volume that reached approximately 3,895 ± 579 mm^3 at the end-point on day 29. Free DOX was able to suppress tumor growth, but the average tumor volume still reached 2,169 ± 427 mm^3 at the end of the treatment period. As compared to the free DOX group, the groups treated with HA-DOX ($P < 0.001$) and HA-DOX/$CaCO_3$ ($P < 0.001$), especially the HA-DOX/$CaCO_3$ group, significantly inhibited tumor progression, and the average tumor volumes of the other two groups were 1,356 ± 227 and 343 ± 73 mm^3 at the end points, respectively. The tumor inhibition rates of the free DOX, HA-DOX, and HA-DOX/$CaCO_3$ groups were 44.3% ± 11.0%, 65.2% ± 5.8%, and 91.2% ± 1.9%, respectively (Fig. 4(c)). Notably, the inhibition rate of

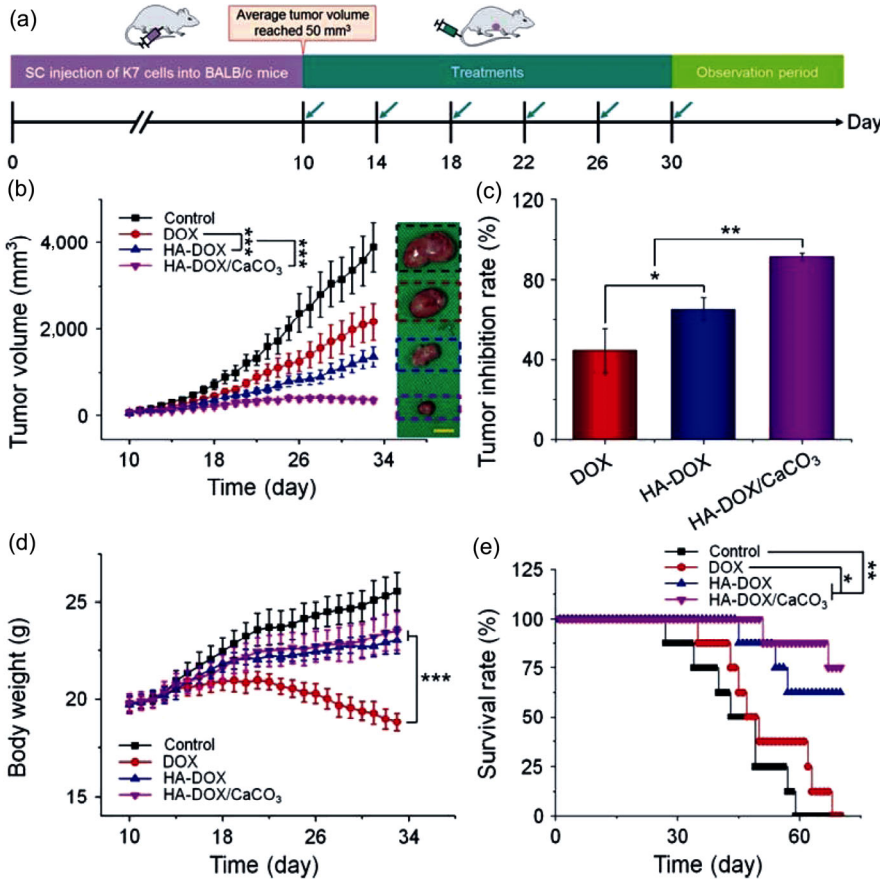

Figure 4 *In vivo* antitumor efficacy in K7 osteosarcoma-allografted mice with an initial tumor volume of 50 mm^3. (a) Experimental schedule for tumor induction and drug treatments. (b) Tumor volumes, (c) tumor inhibition rates, (d) body weight changes, and (e) survival rates of mice treated with free DOX, HA-DOX, and HA-DOX/$CaCO_3$. Scale bar: 1.0 cm. The statistical data are presented as mean ± standard deviation ($n = 10$ for (b)–(d); and $n = 8$ for (e). *$P < 0.05$, **$P < 0.01$, ***$P < 0.001$).

HA-DOX/$CaCO_3$ was 1.4 and 2.1 times higher than that of the free drug and HA-DOX, respectively. As a small molecule, it was difficult to maintain the free DOX treatment condition at the effective DOX concentration in the blood and tumor because of its rapid excretion by glomerular filtration, which therefore limited its antitumor ability. With the improvement of biocompatibility and DOX accumulation in the tumor, HA-DOX/$CaCO_3$ showed an improved tumor inhibition outcome than the other groups ($P < 0.01$).

As presented in Fig. 5(a), free DOX, HA-DOX, or HA-DOX/$CaCO_3$ was administered every four days with an equivalent DOX dosage of 5 $mg \cdot kg^{-1} \cdot BW^{-1}$ for 16 days, and PBS was used as a control. HA-DOX/$CaCO_3$ demonstrated the most efficient tumor suppression in all groups ($P < 0.001$), inhibiting tumor growth by 84.6% ± 1.6% (Figs. 5(b) and 5(c)). Compared with the other groups, this was significantly higher inhibition ($P < 0.01$), which was 2.2 and 1.3 times superior than those of the free DOX group (39.0% ± 8.5%) and HA-DOX (62.9% ± 4.3%) group, respectively. This result was comparable to that obtained in the previous primary osteosarcoma model, and the slightly lower tumor inhibition efficacy might be attributed to the late stage of osteosarcoma with a highly aggressive nature. In addition, survival time was recorded after treatment with PBS, free DOX, HA-DOX, and HA-DOX/$CaCO_3$. As shown in Figs. 4(e) and 5(e), the mice in the groups treated with HA-DOX and especially HA-DOX/$CaCO_3$ revealed a significantly improved survival time than that of the PBS group ($P < 0.01$). However, treatment with free DOX showed no significant amelioration of survival. This can be ascribed to the multiple organ toxicity and consequent body weight decrease, which are concomitant with its antitumor effect. Taken together, HA-DOX/$CaCO_3$ demonstrated remarkably enhanced chemotherapeutic efficacy in tumor inhibition and shows excellent potential for treating both primary and

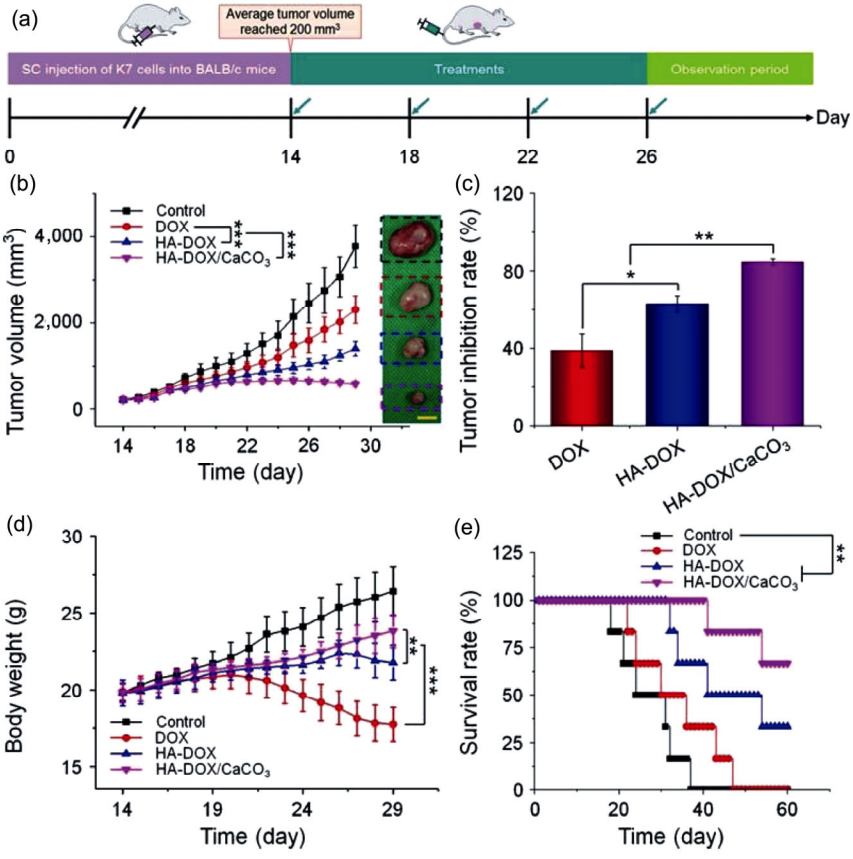

Figure 5 *In vivo* antitumor efficacy in K7 osteosarcoma-allografted mice with an initial tumor volume of 200 mm^3. (a) Experimental schedule for tumor induction and drug treatments. (b) Tumor volumes, (c) tumor inhibition rates, (d) body weight changes, and (e) survival rates of mice treated with PBS as a control, free DOX, HA-DOX, or HA-DOX/$CaCO_3$. Scale bar: 1.0 cm. The statistical data are presented as mean ± standard deviation ($n = 8$ for (b)–(d); and $n = 6$ for (e). *$P < 0.05$, **$P < 0.01$, ***$P < 0.001$).

advanced osteosarcomas.

To further investigate the antitumor efficacy of HA-DOX/$CaCO_3$, the tumors were excised from the mice and sectioned for histopathological analyses at the end point of the treatment. Figure S3(a) in the ESM shows representative H&E-stained images of tumor paraffin sections from the K7 osteosarcoma-allografted mice with an initial tumor volume of ~ 50 mm^3. The control group had an intact tumor structure with more chromatins and binucleated cells, indicating strong cancer cell proliferation [60]. By contrast, various degrees of necrosis in the tumor tissues were detected in the free DOX, HA-DOX, and HA-DOX/$CaCO_3$ groups. In the necrotic area, chromatin was desultorily distributed, and this was quantitatively calculated using the NIS-Elements imaging software (Fig. S3(d) in the ESM) at 90.1% ± 5.7% in the HA-DOX/$CaCO_3$ group, which was 1.4 and 2.2 times larger than those of the free DOX and HA-DOX group, respectively; the necrotic area was only 2.5% ± 0.6% in the control group. This significantly enhanced effect of tumor necrosis ($P < 0.01$) agreed with the *in vivo* tumor inhibition efficiency (Fig. 4(b)). Figure 6(a) shows representative H&E images from the treatment of advanced osteosarcoma, and the result was similar to that observed from the primary treatment model. HA-DOX/$CaCO_3$ induced the greatest degree of tumor cell necrosis

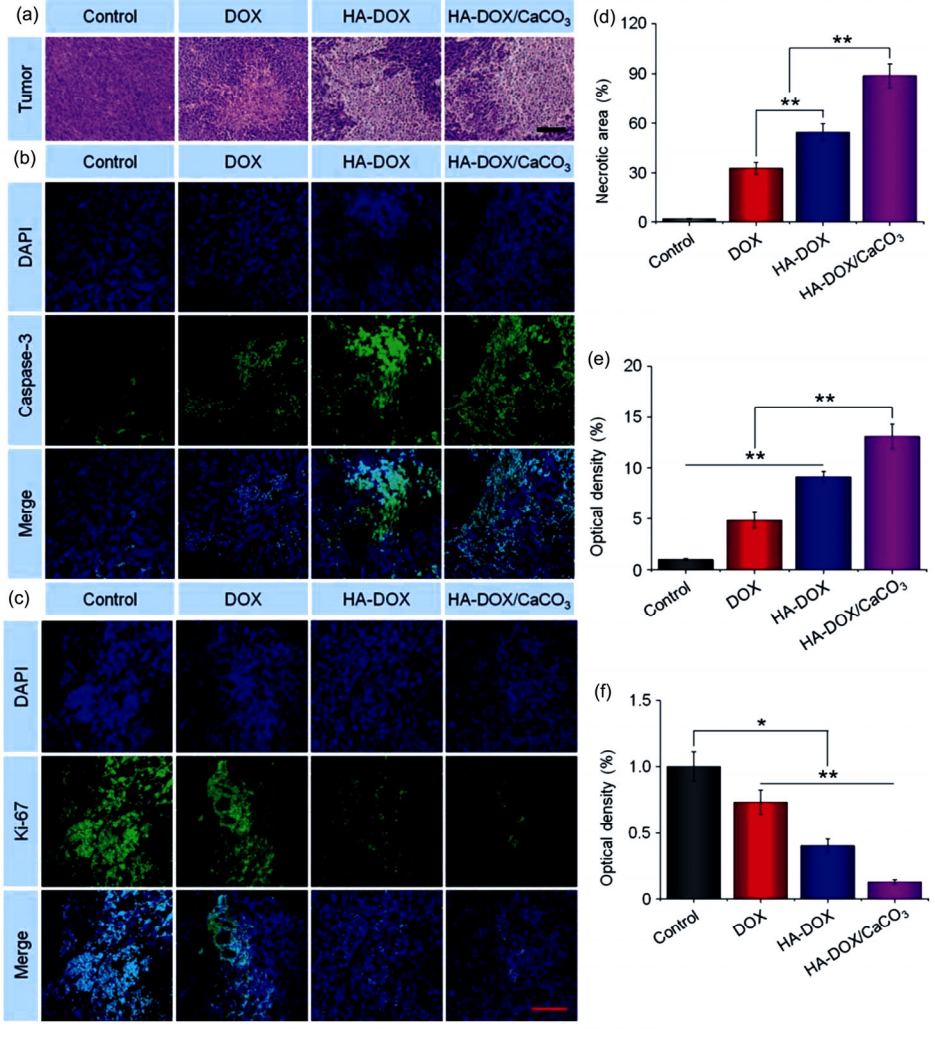

Figure 6 Histopathological and immunohistochemical analyses of tumor sections from the advanced osteosarcoma model. (a) H&E staining and ((b) and (c)) immunofluorescence detection of caspase-3 and Ki-67 of tumor tissue sections from K7 osteosarcoma-allografted BALB/c mice treated with PBS as a control, free DOX, HA-DOX, and HA-DOX/$CaCO_3$. Scale bar: black line = 200.0 μm; red line = 50.0 μm. (d)–(f) Semi-quantitative analyses of tumor necrotic areas from H&E staining, and relative optical densities of immunofluorescence staining of (e) caspase-3 and (f) Ki-67. The statistical data are presented as mean ± standard deviation ($n = 3$ for (d) and (e); $^*P < 0.05$, $^{**}P < 0.01$).

compared with free DOX and HA-DOX. As shown in Fig. 6(d), the necrotic tumor area of the HA-DOX/$CaCO_3$ group was 88.8% ± 7.0%, which was 2.7 and 1.6 times larger than those of the free DOX and HA-DOX groups, respectively ($P < 0.01$). Again, these results indicated that HA-DOX/$CaCO_3$ possessed significantly enhanced antitumor activity.

Caspase-3, a representative marker of the caspase family, is a pivotal mediator of programmed apoptosis [61]. It is also recognized as a "death enzyme" because it is typically activated by numerous death signals [62]. Therefore, the measurement of caspase-3 by immunohistochemistry is widely used to assess the apoptosis level of a cell. Accordingly, we conducted caspase-3 analyses of the tumor tissues from the treated mice. As shown in Fig. S3(b) in the ESM and Fig. 6(b), in both primary and advanced osteosarcoma models, more intensive caspase-3 signals were detected in the tumor tissues of the HA-DOX/$CaCO_3$ group compared with those of the other groups ($P < 0.01$), implying that the HA-DOX/$CaCO_3$ treatment caused more tumor apoptosis.

Ki-67 is a nuclear marker that is also used for assessing the prognosis of cancer patients [63, 64]. Herein, immunohistochemical staining for Ki-67 was performed in tumor sections to investigate the cell proliferation status. As shown in Fig. S3(c) in the ESM, significant tumor cell proliferation was observed in the control group, indicating that the tumor without drug treatment grew aggressively. In contrast, only a few Ki-67-stained cells could be detected in the HA-DOX/$CaCO_3$ group, which was significantly lower than the Ki-67 expression level in both the free DOX and HA-DOX groups. In addition, as presented in Fig. 6(c), the advanced treatment showed a similar trend. This clearly indicated that HA-DOX/$CaCO_3$ could effectively suppress cell proliferation in the tumor tissue and show greatly enhanced antitumor efficacy.

The caspase-3 and Ki-67 signals were further quantified using ImageJ software (National Institutes of Health, Bethesda, Maryland, USA). The relative optical density was calculated as a ratio of the value of the sample to that of the control group (defined as 1). As shown in Fig. S3(e) in the ESM and Fig. 6(e), in both the primary and advanced osteosarcoma models, HA-DOX/$CaCO_3$ induced the highest tumor cell apoptosis rate. The efficacy of apoptosis induced by HA-DOX/$CaCO_3$ was 2.5 and 1.4 times higher than those by of free DOX and HA-DOX in the primary osteosarcoma model, respectively ($P < 0.01$). In the advanced model, HA-DOX/$CaCO_3$ enhanced the cancer cell apoptosis rate by 2.7 and 1.4 times compared with those of free DOX and HA-DOX, respectively ($P < 0.01$). As shown in Fig. S3(f) in the ESM and Fig. 6(f), Ki-67 analyses indicated that HA-DOX/$CaCO_3$ had the strongest inhibitory effect on tumor cell proliferation for treatments of both the primary and advanced osteosarcomas. Specifically, the inhibition efficacy of the tumor cell proliferation of HA-DOX/$CaCO_3$ was 2.0 and 1.1 times higher than those of free DOX and HA-DOX in the primary osteosarcoma model ($P < 0.05$), respectively. A similar result was observed in the advanced osteosarcoma model, and HA-DOX/$CaCO_3$ showed 3.3 and 1.5 times higher efficiency for tumor inhibition compared with the free DOX and HA-DOX groups, respectively ($P < 0.01$).

All of these results demonstrated that HA-DOX/$CaCO_3$ could efficiently inhibit tumor cell growth and increase the apoptosis level *in vivo* for both primary and advanced osteosarcomas, representing an excellent therapeutic effect in osteosarcoma treatment.

2.5 *In vivo* safety of HA-DOX/$CaCO_3$

Serious hemolytic reactions and side effects are the major obstacles that hinder the clinical translation of antitumor drugs. Therefore, it is important to evaluate the safety of HA-DOX/$CaCO_3$ *in vivo*. The *in vivo* biocompatibility of HA-DOX/$CaCO_3$ is a crucial aspect of determining its applicability as an appropriate drug candidate for intravenous injection. First, a hemolysis assay was carried out to estimate the blood compatibility of HA-DOX/$CaCO_3$ [65]. Negligible hemolysis was detected at all of the tested HA-DOX/$CaCO_3$ concentrations up to 1.0 mg·L^{-1} (Fig. 3(b)). The excellent hemocompatibility demonstrated that HA-DOX/$CaCO_3$ is a safe system for intravenous administration without any notable damage to the red blood cell membrane, including disintegration and dissolution.

The body weight change of a mouse during the therapeutic process is a typical indicator reflecting the systemic toxicity of a drug. In this study, the body weight of mice was recorded and analyzed daily. As shown in Figs. 4(d) and 5(d), all of the tumor-bearing mice in the HA-DOX/$CaCO_3$ and HA-DOX groups showed no significant body weight changes over the

whole treatment, which indicated no detectable toxicity. In contrast, the mice treated with free DOX exhibited significant body weight loss over the experimental period ($P < 0.001$). Furthermore, as shown in Fig. 5(d), the HA-DOX/$CaCO_3$ group showed a slighter reduced degree of body weight loss than the HA-DOX group ($P < 0.05$), which may be due to its enhanced tumor-targeting drug release and optimized stability in the blood circulation.

The organ index is another common assessment for *in vivo* toxicity and can reflect the toxicity of drugs toward specific organs. Thus, two mice in each group were randomly euthanized at the end point to extract the heart, liver, spleen, lung, and kidney for organ index analyses by calculating the weight ratio of the organ to the body weight. The HA-DOX and HA-DOX/$CaCO_3$ groups showed similar major organ indices as the control group (Fig. S4(b) in the ESM). However, the spleen index in the free DOX group showed a significant decrease compared to that of the other three groups, which might be due to excess non-selective accumulation and subsequent cell death in the spleen ($P < 0.05$) [66]. A consistent result was obtained in the advanced osteosarcoma model (Fig. 7(b)). These results indicated that HA-DOX and HA-DOX/$CaCO_3$ could effectively reduce organ toxicity via a relatively specific drug delivery route and on-demand drug release.

Furthermore, H&E staining of the main organs (the heart, liver, spleen, lung, and kidney) is commonly used to estimate the long-term toxicity of chemotherapy drugs [67]. As shown in Fig. S4(c) in the ESM, the free DOX significantly damaged the heart by destroying muscle fibers. Additionally, obvious hyperplasia of the alveolar wall and remarkable shrinkage of the renal capsule cavity were observed in the lung and kidney of the free DOX group. In contrast, the two DOX-loaded nanoparticles, especially HA-DOX/$CaCO_3$, caused much less damage to these organs. This might be attributed to the good encapsulation capability and delayed drug release of the nanoparticles under physiological conditions. The resulting lower free drug concentration would be helpful to avoid acute organ damage [68, 69].

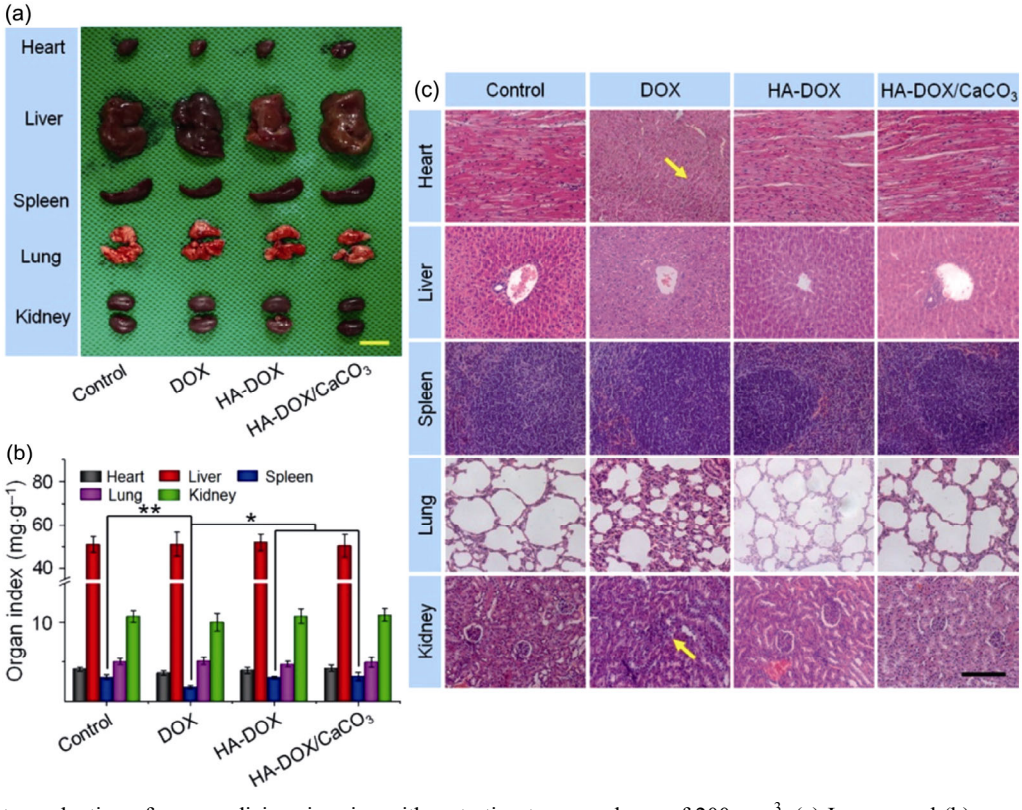

Figure 7 Safety evaluation of nanomedicines in mice with a starting tumor volume of 200 mm^3. (a) Images and (b) organ indices of the major organs of mice treated with free DOX, HA-DOX, and HA-DOX/$CaCO_3$. The yellow scale bar represents 1.0 cm. *$P < 0.05$, **$P < 0.01$. (c) Histopathological analyses of major organs from K7 osteosarcoma-allografted BALB/c mice. The arrows indicate the damaged cardiac muscle fibers, and the shrinking and abnormal glomeruli. The black scale bar represents 200 μm.

A similar conclusion was obtained based on the histopathological analysis shown in Fig. 7(c), further confirming the observation of the *ex vivo* DOX distribution and body weight changes. The encapsulation of DOX by HA-DOX/$CaCO_3$ could protect it from rapid diffusion in the blood circulation and prevent acute organ injury.

3 Conclusions

In summary, a smart tumor microenvironment-responsive HA-$CaCO_3$ hybrid nanoparticle was successfully synthesized via a "green" synthetic method to effectively deliver DOX for osteosarcoma treatment. In normal physiological condition, HA-DOX/$CaCO_3$ was stable with a diameter of 88.2 nm and a restrained DOX release rate of 25.7% ± 5.1% after 72-h incubation, indicating markedly enhanced stability due to crosslinking with $CaCO_3$. When the pH decreased to 5.5, DOX was effectively released with a rapid rate to 89.7% ± 6.4% after 72-h incubation, attributed to the acid-responsive $CaCO_3$ core. Upon systemic injection *in vivo*, HA-DOX/$CaCO_3$ showed effective tumor accumulation. When reaching the tumor tissue, the acidic microenvironment would trigger effective DOX release. In the K7 osteosarcoma-allografted BALB/c mouse model, HA-DOX/$CaCO_3$ demonstrated superior antitumor efficiency with greatly reduced systemic toxicity compared with the free DOX and HA-DOX treatments. Furthermore, HA-DOX/$CaCO_3$ also remarkably improved the survival rate under osteosarcoma treatment. The prominent performance for osteosarcoma treatment with HA-DOX/$CaCO_3$ was also verified at an advanced osteosarcoma stage. Collectively, with convenient fabrication, favorable hemocompatibility and biocompatibility, excellent drug loading, and controlled release properties, HA-DOX/$CaCO_3$ designed in this study holds great potential for chemotherapeutic treatment of various stages of osteosarcoma and is a potential candidate for clinical translation. In addition, our strategy can be extended to other types of cationic small-molecule drugs for the treatment of other diseases.

Acknowledgements

The authors gratefully acknowledge Weiqian Jiang at Yale University for his constructive comments and suggestions. This research was financially supported by the National Natural Science Foundation of China (Nos. 51673190, 51603204, 51473165, 51390484, 81402500, and 51520105004), the National Key Specialty Construction Project of Clinical Pharmacy (No. 30305030698), and the Science and Technology Development Program of Jilin Province (Nos. 20160204015SF and 20160204018SF).

Electronic Supplementary Material: Supplementary material (materials and methods, R_h changes of HA-DOX and HA-DOX/$CaCO_3$ in PBS-buffered BSA and PBS-buffered FBS solutions, zeta potentials of HA-DOX and HA-DOX/$CaCO_3$, histopathological and immunohistochemical analyses of tumor sections from primary osteosarcoma model, safety evaluation of nanomedicines in mice with starting tumor volume of 50 mm^3) is available in the online version of this article at https://doi.org/10.1007/s12274-018-2066-0.

References

[1] Moore, D. D.; Luu, H. H. Osteosarcoma. In *Orthopaedic Oncology*; Peabody, T.; Attar, S., Eds.; Springer: Cham, 2014; pp 65–92.

[2] Gu, X. Y.; Ding, J. X.; Zhang, Z. Y.; Li, Q.; Zhuang, X. L.; Chen, X. S. Polymeric nanocarriers for drug delivery in osteosarcoma treatment. *Curr. Pharm. Des.* **2015**, *21*, 5187–5197.

[3] Isakoff, M. S.; Bielack, S. S.; Meltzer, P.; Gorlick, R. Osteosarcoma: Current treatment and a collaborative pathway to success. *J. Clin. Oncol.* **2015**, *33*, 3029–3035.

[4] Kansara, M.; Teng, M. W.; Smyth, M. J.; Thomas, D. M. Translational biology of osteosarcoma. *Nat. Rev. Cancer* **2014**, *14*, 722–735.

[5] Shen, G. Z.; Xing, R. R.; Zhang, N.; Chen, C. J.; Ma, G. H.; Yan, X. H. Interfacial cohesion and assembly of bioadhesive molecules for design of long-term stable hydrophobic nanodrugs toward effective anticancer therapy. *ACS Nano* **2016**, *10*, 5720–5729.

[6] He, L.; Li, D.; Wang, Z. T.; Xu, W. G.; Wang, J. X.; Guo, H.; Wang, C. X.; Ding, J. X. L-Cystine-crosslinked polypeptide nanogel as a reduction-responsive excipient for prostate cancer chemotherapy. *Polymers* **2016**, *8*, 36.

[7] Li, D.; Xu, W. G.; Li, P. Q.; Ding, J. X.; Cheng, Z. L.; Chen, L.; Yan, L. S.; Chen, X. S. Self-targeted polysaccharide prodrug suppresses orthotopic hepatoma. *Mol. Pharmaceutics* **2016**, *13*, 4231–4235.

[8] Chen, J. J.; Ding, J. X.; Wang, Y. C.; Cheng, J. J.; Ji, S. X.; Zhuang, X. L.; Chen, X. S. Sequentially responsive shell-stacked nanoparticles for deep penetration into solid tumors. *Adv. Mater.* **2017**, *29*, 1701170.

[9] Sun, W. J.; Jiang, T. Y.; Lu, Y.; Reiff, M.; Mo, R.; Gu, Z. Cocoon-like self-degradable DNA nanoclew for anticancer drug delivery. *J. Am. Chem. Soc.* **2014**, *136*, 14722−14725.

[10] Mo, R.; Jiang, T. Y.; DiSanto, R.; Tai, W. Y.; Gu, Z. ATP-triggered anticancer drug delivery. *Nat. Commun.* **2014**, *5*, 3364.

[11] Jiang, T. Y.; Sun, W. J.; Zhu, Q. W.; Burns, N. A.; Khan, S. A.; Mo, R.; Gu, Z. Furin-mediated sequential delivery of anticancer cytokine and small-molecule drug shuttled by graphene. *Adv. Mater.* **2015**, *27*, 1021−1028.

[12] Wang, C.; Xu, L. G.; Liang, C.; Xiang, J.; Peng, R.; Liu, Z. Immunological responses triggered by photothermal therapy with carbon nanotubes in combination with anti-CTLA-4 therapy to inhibit cancer metastasis. *Adv. Mater.* **2014**, *26*, 8154−8162.

[13] de Faria, P. C. B.; dos Santos, L. I.; Coelho, J. P.; Ribeiro, H. B.; Pimenta, M. A.; Ladeira, L. O.; Gomes, D. A.; Furtado, C. A.; Gazzinelli, R. T. Oxidized multiwalled carbon nanotubes as antigen delivery system to promote superior $CD8^+$ T cell response and protection against cancer. *Nano Lett.* **2014**, *14*, 5458−5470.

[14] Allen, T. M.; Cullis, P. R. Liposomal drug delivery systems: From concept to clinical applications. *Adv. Drug Del. Rev.* **2013**, *65*, 36−48.

[15] Chen, Q.; Feng, L. Z.; Liu, J. J.; Zhu, W. W.; Dong, Z. L.; Wu, Y. F.; Liu, Z. Intelligent albumin–MnO_2 nanoparticles as pH-/H_2O_2-responsive dissociable nanocarriers to modulate tumor hypoxia for effective combination therapy. *Adv. Mater.* **2016**, *28*, 7129−7136.

[16] Feng, X. R.; Ding, J. X.; Gref, R.; Chen, X. S. Poly(β-cyclodextrin)-mediated polylactide-cholesterol stereocomplex micelles for controlled drug delivery. *Chin. J. Polym. Sci.* **2017**, *35*, 693−699.

[17] Zhang, X. D.; Liang, X.; Gu, J. J.; Chang, D. F.; Zhang, J. X.; Chen, Z. W.; Ye, Y. Q.; Wang, C.; Tao, W.; Zeng, X. W. et al. Investigation and intervention of autophagy to guide cancer treatment with nanogels. *Nanoscale* **2017**, *9*, 150−163.

[18] Qian, C. G.; Yu, J. C.; Chen, Y. L.; Hu, Q. Y.; Xiao, X. Z.; Sun, W. J.; Wang, C.; Feng, P. J.; Shen, Q. D.; Gu, Z. Light-activated hypoxia-responsive nanocarriers for enhanced anticancer therapy. *Adv. Mater.* **2016**, *28*, 3313−3320.

[19] Zhang, Y.; Wang, F.; Li, M.; Yu, Z.; Qi, R.; Ding, J.; Zhang, Z.; Chen, X. Self-stabilized hyaluronate nanogel for intracellular codelivery of doxorubicin and cisplatin to osteosarcoma. *Adv. Sci.* **2018**, 1700821.

[20] Li, M. Q.; Tang, Z. H.; Zhang, D. W.; Sun, H.; Liu, H. Y.; Zhang, Y.; Zhang, Y. Y.; Chen, X. S. Doxorubicin-loaded polysaccharide nanoparticles suppress the growth of murine colorectal carcinoma and inhibit the metastasis of murine mammary carcinoma in rodent models. *Biomaterials* **2015**, *51*, 161−172.

[21] Ma, X. M.; Zhang, X. T.; Yang, L.; Wang, G.; Jiang, K.; Wu, G.; Cui, W. G.; Wei, Z. P. Tunable construction of multi-shelled hollow carbonate nanospheres and their potential applications. *Nanoscale* **2016**, *8*, 8687−8695.

[22] Wei, W.; Ma, G. H.; Hu, G.; Yu, D.; McLeish, T.; Su, Z. G.; Shen, Z. Y. Preparation of hierarchical hollow $CaCO_3$ particles and the application as anticancer drug carrier. *J. Am. Chem. Soc.* **2008**, *130*, 15808−15810.

[23] Dong, Z. L.; Feng, L. Z.; Zhu, W. W.; Sun, X. Q.; Gao, M.; Zhao, H.; Chao, Y.; Liu, Z. $CaCO_3$ nanoparticles as an ultra-sensitive tumor-pH-responsive nanoplatform enabling real-time drug release monitoring and cancer combination therapy. *Biomaterials* **2016**, *110*, 60−70.

[24] Dong, Z. L.; Feng, L. Z.; Hao, Y.; Chen, M. C.; Gao, M.; Chao, Y.; Zhao, H.; Zhu, W. W.; Liu, J. J.; Liang, C. et al. Synthesis of hollow biomineralized $CaCO_3$–polydopamine nanoparticles for multimodal imaging-guided cancer photodynamic therapy with reduced skin photosensitivity. *J. Am. Chem. Soc.* **2018**, *140*, 2165−2178.

[25] Gonçalves, M.; Maciel, D.; Capelo, D.; Xiao, S. L.; Sun, W. J.; Shi, X. Y.; Rodrigues, J.; Tomás, H.; Li, Y. L. Dendrimer-assisted formation of fluorescent nanogels for drug delivery and intracellular imaging. *Biomacromolecules* **2014**, *15*, 492−499.

[26] Liang, P.; Zhao, D.; Wang, C. Q.; Zong, J. Y.; Zhuo, R. X.; Cheng, S. X. Facile preparation of heparin/$CaCO_3$/CaP hybrid nano-carriers with controllable size for anticancer drug delivery. *Colloids Surf. B Biointerfaces* **2013**, *102*, 783−788.

[27] Han, S. Y.; Han, H. S.; Lee, S. C.; Kang, Y. M.; Kim, I. S.; Park, J. H. Mineralized hyaluronic acid nanoparticles as a robust drug carrier. *J. Mater. Chem.* **2011**, *21*, 7996−8001.

[28] Min, K. H.; Min, H. S.; Lee, H. J.; Park, D. J.; Yhee, J. Y.; Kim, K.; Kwon, I. C.; Jeong, S. Y.; Silvestre, O. F.; Chen, X. Y. et al. pH-controlled gas-generating mineralized nanoparticles: A theranostic agent for ultrasound imaging and therapy of cancers. *ACS Nano* **2015**, *9*, 134−145.

[29] Ma, X. M.; Chen, H. F.; Yang, L.; Wang, K.; Guo, Y. M.; Yuan, L. Construction and potential applications of a functionalized cell with an intracellular mineral scaffold. *Angew. Chem., Int. Ed.* **2011**, *50*, 7414−7417.

[30] Zhao, Y.; Luo, Z.; Li, M. H.; Qu, Q. Y.; Ma, X.; Yu, S. H.; Zhao, Y. L. A preloaded amorphous calcium carbonate/doxorubicin@silica nanoreactor for pH-responsive delivery of an anticancer drug. *Angew. Chem., Int. Ed.* **2015**, *54*, 919−922.

[31] Ding, J.; Liang, T.; Zhou, Y.; He, Z. W.; Min, Q. H.; Jiang, L. P.; Zhu, J. J. Hyaluronidase-triggered anticancer drug and sirna

delivery from cascaded targeting nanoparticles for drug-resistant breast cancer therapy. *Nano Res.* **2017**, *10*, 690−703.

[32] Zhang, Y.; Wu, K. Q.; Sun, H. L.; Zhang, J.; Yuan, J. D.; Zhong, Z. Y. Hyaluronic acid-shelled disulfide-cross-linked nanopolymersomes for ultrahigh-efficiency reactive encapsulation and CD44-targeted delivery of mertansine toxin. *ACS Appl. Mater. Interfaces* **2018**, *10*, 1597−1604.

[33] Chen, W. S.; Ouyang, J.; Liu, H.; Chen, M.; Zeng, K.; Sheng, J. P.; Liu, Z. J.; Han, Y. J.; Wang, L. Q.; Li, J. et al. Black phosphorus nanosheet-based drug delivery system for synergistic photodynamic/photothermal/chemotherapy of cancer. *Adv. Mater.* **2017**, *29*, 1603864.

[34] Xu, W. G.; Ding, J. X.; Xiao, C. S.; Li, L. Y.; Zhuang, X. L.; Chen, X. S. Versatile preparation of intracellular-acidity-sensitive oxime-linked polysaccharide-doxorubicin conjugate for malignancy therapeutic. *Biomaterials* **2015**, *54*, 72−86.

[35] Li, C.; Qian, M.; Wang, S.; Jiang, H.; Du, Y.; Wang, J.; Lu, W.; Murthy, N.; Huang, R. Aptavalve-gated mesoporous carbon nanospheres image cellular mucin and provide on-demand targeted drug delivery. *Theranostics* **2017**, *7*, 3319−3325.

[36] Han, X. P.; Li, Z. B.; Sun, J.; Luo, C.; Li, L.; Liu, Y. H.; Du, Y. Q.; Qiu, S. H.; Ai, X. Y.; Wu, C. N. et al. Stealth CD44-targeted hyaluronic acid supramolecular nanoassemblies for doxorubicin delivery: Probing the effect of uncovalent pegylation degree on cellular uptake and blood long circulation. *J. Controlled Release* **2015**, *197*, 29−40.

[37] Li, S. Y.; Liu, L. H.; Cheng, H.; Li, B.; Qiu, W. X.; Zhang, X. Z. A dual-FRET-based fluorescence probe for the sequential detection of MMP-2 and caspase-3. *Chem. Commun.* **2015**, *51*, 14520−14523.

[38] Mo, R.; Gu, Z. Tumor microenvironment and intracellular signal-activated nanomaterials for anticancer drug delivery. *Mater. Today* **2016**, *19*, 274−283.

[39] Hu, Q. Y.; Sun, W. J.; Lu, Y.; Bomba, H. N.; Ye, Y. Q.; Jiang, T. Y.; Isaacson, A. J.; Gu, Z. Tumor microenvironment-mediated construction and deconstruction of extracellular drug-delivery depots. *Nano Lett.* **2016**, *16*, 1118−1126.

[40] Alvarez-Lorenzo, C.; Blanco-Fernandez, B.; Puga, A. M.; Concheiro, A. Crosslinked ionic polysaccharides for stimuli-sensitive drug delivery. *Adv. Drug Del. Rev.* **2013**, *65*, 1148−1171.

[41] Li, M. Q.; Lv, S. X.; Tang, Z. H.; Song, W. T.; Yu, H. Y.; Sun, H.; Liu, H. Y.; Chen, X. S. Polypeptide/doxorubicin hydrochloride polymersomes prepared through organic solvent-free technique as a smart drug delivery platform. *Macromol. Biosci.* **2013**, *13*, 1150−1162.

[42] Li, S. Y.; Zhang, T.; Xu, W. G.; Ding, J. X.; Yin, F.; Xu, J.; Sun, W.; Wang, H. S.; Sun, M. X.; Cai, Z. D. Sarcoma-targeting peptide-decorated polypeptide nanogel intracellularly delivers shikonin for upregulated osteosarcoma necroptosis and diminished pulmonary metastasis. *Theranostics* **2018**, *8*, 1361−1375.

[43] Jiang, Q.; Nie, Y.; Chen, X. B.; He, Y. Y.; Yue, D.; Gu, Z. W. pH-triggered pinpointed cascading charge-conversion and redox-controlled gene release design: Modularized fabrication for nonviral gene transfection. *Adv. Funct. Mater.* **2017**, *27*, 1701571.

[44] Lei, M.; Fu, C.; Cheng, X.; Fu, B.; Wu, N. N.; Zhang, Q.; Fu, A. L.; Cheng, J. L.; Gao, J. H.; Zhao, Z. H. Activated surface charge-reversal manganese oxide nanocubes with high surface-to-volume ratio for accurate magnetic resonance tumor imaging. *Adv. Funct. Mater.* **2017**, *27*, 1700978.

[45] Zhang, Y.; Xiao, C. S.; Li, M. Q.; Ding, J. X.; He, C. L.; Zhuang, X. L.; Chen, X. S. Core-cross-linked micellar nanoparticles from a linear-dendritic prodrug for dual-responsive drug delivery. *Polym. Chem.* **2014**, *5*, 2801−2808.

[46] He, Q.; Huang, S.; Xu, S. Y.; Wang, L. Y. pH-responsive cocktail drug nanocarriers by encapsulating paclitaxel with doxorubicin modified poly(amino acid). *RSC Adv.* **2015**, *5*, 43148−43154.

[47] McGowan, J. V.; Chung, R.; Maulik, A.; Piotrowska, I.; Walker, J. M.; Yellon, D. M. Anthracycline chemotherapy and cardiotoxicity. *Cardiovasc. Drugs Ther.* **2017**, *31*, 63−75.

[48] Zhao, Y. Y.; Chen, F.; Pan, Y. M.; Li, Z. P.; Xue, X. D.; Okeke, C. I.; Wang, Y. F.; Li, C.; Peng, L.; Wang, P. C. et al. Nanodrug formed by coassembly of dual anticancer drugs to inhibit cancer cell drug resistance. *ACS Appl. Mater. Interfaces* **2015**, *7*, 19295−19305.

[49] Lee, S. M.; O'Halloran, T. V.; Nguyen, S. T. Polymer-caged nanobins for synergistic cisplatin−doxorubicin combination chemotherapy. *J. Am. Chem. Soc.* **2010**, *132*, 17130−17138.

[50] Zhang, W. J.; Wang, F. H.; Wang, Y.; Wang, J. N.; Yu, Y. N.; Guo, S. R.; Chen, R. J.; Zhou, D. J. pH and near-infrared light dual-stimuli responsive drug delivery using DNA-conjugated gold nanorods for effective treatment of multidrug resistant cancer cells. *J. Controlled Release* **2016**, *232*, 9−19.

[51] Wang, C.; Wu, C. Y.; Zhou, X. J.; Han, T.; Xin, X. Z.; Wu, J. Y.; Zhang, J. Y.; Guo, S. W. Enhancing cell nucleus accumulation and DNA cleavage activity of anti-cancer drug via graphene quantum dots. *Sci. Rep.* **2013**, *3*, 2852.

[52] Farhane, Z.; Bonnier, F.; Byrne, H. J. Monitoring doxorubicin cellular uptake and trafficking using *in vitro* Raman microspectroscopy: Short and long time exposure effects on lung cancer cell lines. *Anal. Bioanal. Chem.* **2017**, *409*, 1333−1346.

[53] Zhao, K. D.; Li, D.; Xu, W. G.; Ding, J. X.; Jiang, W. Q.; Li, M. Q.; Wang, C. X.; Chen, X. S. Targeted hydroxyethyl starch prodrug for inhibiting the growth and metastasis of prostate cancer. *Biomaterials* **2017**, *116*, 82−94.

[54] Jin, E. L.; Zhang, B.; Sun, X. R.; Zhou, Z. X.; Ma, X. P.; Sun, Q. H.; Tang, J. B.; Shen, Y. Q.; Van Kirk, E.; Murdoch, W. J. et al.

Acid-active cell-penetrating peptides for *in vivo* tumor-targeted drug delivery. *J. Am. Chem. Soc.* **2013**, *135*, 933−940.

[55] Ding, J. X.; Xu, W. G.; Zhang, Y.; Sun, D. K.; Xiao, C. S.; Liu, D. H.; Zhu, X. J.; Chen, X. S. Self-reinforced endocytoses of smart polypeptide nanogels for "on-demand" drug delivery. *J. Controlled Release* **2013**, *172*, 444−455.

[56] Lv, S. X.; Tang, Z. H.; Li, M. Q.; Lin, J.; Song, W. T.; Liu, H. Y.; Huang, Y. B.; Zhang, Y. Y.; Chen, X. S. Co-delivery of doxorubicin and paclitaxel by PEG-polypeptide nanovehicle for the treatment of non-small cell lung cancer. *Biomaterials* **2014**, *35*, 6118−6129.

[57] Li, M. Q.; Tang, Z. H.; Lv, S. X.; Song, W. T.; Hong, H.; Jing, X. B.; Zhang, Y. Y.; Chen, X. S. Cisplatin crosslinked pH-sensitive nanoparticles for efficient delivery of doxorubicin. *Biomaterials* **2014**, *35*, 3851−3864.

[58] Kang, M. S.; Singh, R. K.; Kim, T. H.; Kim, J. H.; Patel, K. D.; Kim, H. W. Optical imaging and anticancer chemotherapy through carbon dot created hollow mesoporous silica nanoparticles. *Acta Biomater.* **2017**, *55*, 466−480.

[59] Tao, X. Y.; Jia, N.; Cheng, N. H.; Ren, Y. H.; Cao, X. N.; Liu, M.; Wei, D. Z.; Wang, F. Q. Design and evaluation of a phospholipase d based drug delivery strategy of novel phosphatidyl-prodrug. *Biomaterials* **2017**, *131*, 1−14.

[60] Li, M. Q.; Tang, Z. H.; Zhang, Y.; Lv, S. X.; Li, Q. S.; Chen, X. S. Targeted delivery of cisplatin by LHRH-peptide conjugated dextran nanoparticles suppresses breast cancer growth and metastasis. *Acta Biomater.* **2015**, *18*, 132−143.

[61] Murthy, A.; Li, Y.; Peng, I.; Reichelt, M.; Katakam, A. K.; Noubade, R.; Roose-Girma, M.; DeVoss, J.; Diehl, L.; Graham, R. R. et al. A Crohn's disease variant in *Atg16l1* enhances its degradation by caspase 3. *Nature* **2014**, *506*, 456−462.

[62] Okada, H.; Mak, T. W. Pathways of apoptotic and non-apoptotic death in tumour cells. *Nat. Rev. Cancer* **2004**, *4*, 592−603.

[63] Wentzensen, N.; Schwartz, L.; Zuna, R. E.; Smith, K.; Mathews, C.; Gold, M. A.; Allen, R. A.; Zhang, R.; Dunn, S. T.; Walker, J. L. et al. Performance of p16/Ki-67 immunostaining to detect cervical cancer precursors in a colposcopy referral population. *Clin. Cancer Res.* **2012**, *18*, 4154−4162.

[64] Bertz, S.; Otto, W.; Denzinger, S.; Wieland, W. F.; Burger, M.; Stöhr, R.; Link, S.; Hofstädter, F.; Hartmann, A. Combination of CK20 and Ki-67 immunostaining analysis predicts recurrence, progression, and cancer-specific survival in pt1 urothelial bladder cancer. *Eur. Urol.* **2014**, *65*, 218−226.

[65] Sun, D. K.; Ding, J. X.; Xiao, C. S.; Chen, J. J.; Zhuang, X. L.; Chen, X. S. Preclinical evaluation of antitumor activity of acid-sensitive pegylated doxorubicin. *ACS Appl. Mater. Interfaces* **2014**, *6*, 21202−21214.

[66] Miranda, C. J.; Makui, H.; Soares, R. J.; Bilodeau, M.; Mui, J.; Vali, H.; Bertrand, R.; Andrews, N. C.; Santos, M. M. Hfe deficiency increases susceptibility to cardiotoxicity and exacerbates changes in iron metabolism induced by doxorubicin. *Blood* **2003**, *102*, 2574−2580.

[67] Ding, J. X.; Li, C.; Zhang, Y.; Xu, W. G.; Wang, J.; Chen, X. Chirality-mediated polypeptide micelles for regulated drug delivery. *Acta Biomater.* **2015**, *11*, 346−355.

[68] Han, K.; Zhang, W. Y.; Zhang, J.; Ma, Z. Y.; Han, H. Y. pH-responsive nanoscale coordination polymer for efficient drug delivery and real-time release monitoring. *Adv. Healthcare Mater.* **2017**, *6*, 1700470.

[69] Li, X. R.; Yang, X. C.; Lin, Z. Q.; Wang, D.; Mei, D.; He, B.; Wang, X. Y.; Wang, X. Y.; Zhang, Q.; Gao, W. A folate modified pH sensitive targeted polymeric micelle alleviated systemic toxicity of doxorubicin (DOX) in multi-drug resistant tumor bearing mice. *Eur. J. Pharm. Sci.* **2015**, *76*, 95−101.